Non-intrusive reduced order modeling of fluid-structure interactions

D. Xiao[a,b], P.Yang[a], F. Fang[a,*], J. Xiang[a], C.C. Pain[a], I.M. Navon[c]

[a]*Applied Modelling and Computation Group, Department of Earth Science and Engineering,Imperial College London, Prince Consort Road, London, SW7 2BP, UK.URL:* `http://amcg.ese.imperial.ac.uk`
[b]*China University of Geosciences, Wuhan, 430074, China*
[c]*Department of Scientific Computing, Florida State University,Tallahassee, FL, 32306-4120, USA*

Abstract

A novel non-intrusive reduced order model (NIROM) for fluid-structure interaction (FSI) has been developed. The model is based on proper orthogonal decomposition (POD) and radial basis function (RBF) interpolation method. The method is independent of the governing equations, therefore, it does not require modifications to the source code. This is the first time that a NIROM was constructed for FSI phenomena using POD and RBF interpolation method. Another novelty of this work is the first implementation of the FSI NIROM under the framework of an unstructured mesh finite element multi-phase model (Fluidity) and a combined finite-discrete element method based solid model (Y2D).

The capability of this new NIROM for FSI is numerically illustrated in three coupling simulations: a one-way coupling case (flow past a cylinder), a two-way coupling case (a free-falling cylinder in water) and a vortex-induced vibrations of a elastic beam test case. It is shown that the FSI NIROM results in a large CPU time reduction by several orders of magnitude while the dominant details of the high fidelity model are captured.

Keywords: RBF, POD, fluid-structure interaction, non-intrusive, coupling

1. Introduction

Fluid-structure interaction is an interaction phenomena between deformable or movable solid structures with a surrounding or internal fluid flow [1]. The FSI problem plays an important role in many scientific and engineering areas such as aerospace wings design, biology, turbomachinery and blood flow in veins and arteries. However, the computational cost for simulating the FSI problem is intensive. In this paper a new reduced order modelling method is presented to resolve complex FSI problems at a low computational cost.

*Corresponding author
Email address: `f.fang@imperial.ac.uk` (F. Fang)

Over the past decades, the reduced order modelling method has proven to be a powerful tool of reducing the dimension of large dynamic systems. Among model reduction techniques, the proper orthogonal decomposition (POD) is the most widely used method. POD is capable of representing large systems using a few number of optimal basis functions and it has been applied successfully to various research and engineering fields such as ocean models [2], air pollution [3], mesh optimization [4], shape optimization problems [5], porous media [6, 7], shallow water [8, 9, 10], aerospace design [11] and neutron/photon transport problems [12].

In POD reduced order modelling, Galerkin projection methods are usually used to generate a reduced order model (ROM) by projecting the governing equations onto POD bases [13]. However, the main issues in reduced order modelling are stability and non-linear inefficiency [14, 15, 16, 17]. Various stabilisation methods have been proposed such as Petrov-Galerkin method [2, 18], calibration [19, 20], regularisation [21] and Fourier expansion [22]. A number of non-linearity treatment methods have also been presented, including empirical interpolation method (EIM) [23], discrete empirical interpolation method (DEIM) [17], residual DEIM (RDEIM) [24], Petrov−Galerkin projection method [19], Gauss−Newton with approximated tensors method (GNAT) [25] and the quadratic expansion method [26, 27].

Recently, the reduced order modelling method has been applied to fluid-structure interaction problem [28, 29, 30, 31, 32, 33]. However, those methods are dependent on the governing equations, that is, they are intrusive ROMs. The disadvantage of intrusive ROMs is that the source code describing the physical system has to be modified in order to construct the ROM. The modifications could be complex or may be impossible if the source code is unavailable (*e.g.* in commercial software) [34]. To overcome this disadvantage, various non-intrusive reduced order modelling (NIROM) methods have been proposed. Xiao et al. proposed a non-intrusive ROM for the Navier-Stokes equations using the POD and Smolyak sparse grid interpolation methods[35]. This method constructs a hyper surface that replaces the equations of reduced system. Chen et al. proposed a non-intrusive ROM based on black-box stencil interpolation method [34]. Walton et al. proposed one for unsteady fluid flow using radial basis function (RBF) interpolation and POD [36]. Audouze et al. proposed a two-level non-intrusive reduced order modelling approach for nonlinear parametrized time-dependent PDEs using RBF and POD [37, 38]. Xiao *et al.* also presented a non-intrusive reduced order method for Navier-Stokes equations using POD and RBF interpolation [39].

This paper uses, for the first time, the non-intrusive method to derive a reduced order model for fluid-structure interaction problems using the POD and RBF methods. This has been implemented under the framework of an unstructured mesh finite element model (Fluidity) and a combined finite-discrete element solid model (Y2D). The novelty of this work lies in the use of non-intrusive method to represent solutions of fluid-structure interaction problems on reduced spaces.

In this approach, the solutions to the high fidelity model are recorded as a sequence of snapshots and a number of POD bases are generated through these snapshots that optimally represent the fluid-structure interaction problem. The RBF multi-dimensional interpolation method is then used to construct a hyper-surface that represents the FSI ROM. After obtaining the hyper-surface, the solution of the new FSI ROM at the current time levels can be calculated through inputting POD coefficients at earlier time

levels into this hyper-surface. The capability of the new fluid-structure interaction reduced order model (FSI NIROM) has been assessed through three coupling test cases: a one-way coupling test case - flow past a cylinder, a two-way coupling test case - a free-falling cylinder in water- and the case - vortex-induced vibration of a elastic beam. Comparisons between the high fidelity full model and the proposed FSI NIROM are made to validate the accuracy of the new FSI NIROM.

The structure of the paper is as follows: section 2 presents the governing equations of fluid-structure interaction problems; section 3 derives the methods of constructing a non-intrusive reduced order model for fluid-structure interaction problems using the FSI NIROM method; section 4 demonstrates the capability of the derived methodology by three numerical examples: a one-way coupling test case(flow past a cylinder), a two-way coupling test case(a free-falling cylinder in water) and a vortex-induced vibrations of a elastic beam test case; Finally in section 5, summary and conclusions are presented.

2. Governing equations

In this section, the governing equations of the fluid-structure interaction are described, which consist of governing equations for fluid dynamics and solid dynamics.

2.1. Governing equations for fluid dynamics

The Navier-Stokes equations are used for fluid dynamics:

$$\nabla \cdot \boldsymbol{u}_f = 0, \tag{1}$$

$$\rho_f \frac{D\boldsymbol{u}_f}{Dt} = \nabla \cdot \tau - \nabla p + \boldsymbol{B}_f, \tag{2}$$

where $\boldsymbol{u}_f$ denotes velocity vector of fluids, τ the viscous forces, p the pressure and $\boldsymbol{B_f}$ the body forces (*e.g.* gravity force). The ρ_f is the density of fluids.

2.2. Governing equations for solid dynamics

The governing equation of solid dynamics is the Newton's second law and has the discretised form as follows:

$$\boldsymbol{F}_{external} + \boldsymbol{F}_{viscosity} + \boldsymbol{F}_{pressure} + \boldsymbol{F}_{contact} - \boldsymbol{F}_{internal} = M\frac{\partial \boldsymbol{u}_s}{\partial t}, \tag{3}$$

where M denotes the mass matrix of nodes and it is given by $\boldsymbol{M} = \int_{V_0} \rho_0 \boldsymbol{N}\boldsymbol{N}^T dV$ (ρ_0 being the density of solids and $\boldsymbol{N}$ being finite element basis function), $\boldsymbol{F}_{internal}$ is the internal force and it is obtained by $\boldsymbol{F}_{internal} = \int_{v^{(n)}} \frac{\partial \boldsymbol{N}}{\partial \boldsymbol{x}} \boldsymbol{T} dv$ ($\boldsymbol{T}$ being the Cauchy stress). The $\boldsymbol{F}_{external}$ is the external force and derived by $\boldsymbol{F}_{external} = \int_{v^{(e)}} \boldsymbol{N}\boldsymbol{b} dv + \int_{v^{(e)}} \boldsymbol{N}\boldsymbol{t} dv$ ($\boldsymbol{b}$ being the body force, $\boldsymbol{t}$ being surface traction force). $\boldsymbol{F}_{viscosity}$ and $\boldsymbol{F}_{pressure}$ are viscous force and pressure at the fluid-solid interface respectively. In one way coupling, $\boldsymbol{F}_{viscosity} = 0$. The $\boldsymbol{F}_{contact}$ denotes the contact force between solids, for details, see Munjiza [40].

2.3. Fluid-solid Coupling equations

In this article, the Navier-Stokes equations are used for resolving the problem on the extended computational domain (Ω) comprised of the fluid Ω_f and solid Ω_s domains. In order to couple the fluid and solid, a supplementary equation is introduced:

$$\frac{\rho_f}{\Delta t}(\hat{\boldsymbol{u}}^f - \boldsymbol{u}_f^f) = \frac{\rho_f}{\Delta t}(\boldsymbol{u}_s^s - \boldsymbol{u}_f^s), \tag{4}$$

where $\boldsymbol{u}$ is the velocity, the subscripts denote material field (*i.e.* s denotes solid and f denotes fluid) while the superscripts denote material to which mesh is associated (*i.e.* s denotes values on the solid mesh and f denotes values on the fluid mesh) and $\hat{\boldsymbol{u}}^f$ is the bulk velocity which has the following form:

$$\hat{\boldsymbol{u}}^f = \alpha_f \boldsymbol{u}_f^f + \alpha_s \boldsymbol{u}_s^f = \hat{\boldsymbol{u}}_f^f + \hat{\boldsymbol{u}}_s^f, \tag{5}$$

and

$$\hat{\boldsymbol{u}}^f = \begin{cases} \boldsymbol{u}_f^f & \text{if } \alpha_f = 1, \alpha_s = 0 \\ \boldsymbol{u}_s^f & \text{if } \alpha_f = 0, \alpha_s = 1 \end{cases} \tag{6}$$

where α_f and α_s are the volume fractions for the fluid and solid respectively, and $\alpha_f + \alpha_s$=1,

The continuity equation (1) on the extended computational domain ($\Omega = \Omega_f \cup \Omega_s$) then has the form of:

$$\nabla \cdot \hat{\boldsymbol{u}}^f = \nabla \cdot (\hat{\boldsymbol{u}}_f^f + \hat{\boldsymbol{u}}_s^f) = 0. \tag{7}$$

In order to obtain the solutions of the coupled system, the velocity of solids on the solid mesh, $\boldsymbol{u}_s^s$, is projected onto the fluid mesh, then it becomes $\hat{\boldsymbol{u}}_s^f$ [41].

To represent the impact of solid-fluid interactions on fluid solutions, a source term $\boldsymbol{s}_c^f$ is introduced into the momentum equation (2), that is:

$$\rho_f \frac{D\boldsymbol{u}_f}{Dt} = \nabla \cdot \tau - \nabla p + \boldsymbol{s}_c^f, \tag{8}$$

where σ_f denotes the total stress tensor which considers the contribution of pressure and $\boldsymbol{B_f}$ is the body forces (*e.g.* gravity force). $\boldsymbol{s}_c^f$ is the source term considering exchange forces between the fluid and solid for the sake of viscous terms and it consists of three components, that is, $\boldsymbol{s}_c^f = (\boldsymbol{s}_{c,x}^f, \boldsymbol{s}_{c,y}^f, \boldsymbol{s}_{c,z}^f)^T$, for details, see [42].

2.3.1. One way coupling

In one way coupling, the following equations are used:

$$\boldsymbol{F}_{pressure}^s = \int_{\Gamma_{solid}} \boldsymbol{N}_i \boldsymbol{n} \cdot (Ip) d\Gamma, \tag{9}$$

$$\boldsymbol{s}_c^f = (\boldsymbol{s}_{c,x}^f, \boldsymbol{s}_{c,y}^f, \boldsymbol{s}_{c,z}^f)^T = 0, \tag{10}$$

where N_i denotes the finite element basis function over element i. $\boldsymbol{n}$ is the unit normal vector on the solid surface $\boldsymbol{n} = (n_x, n_y, n_z)$. I is a unit diagonal matrix and p is pressure.

2.3.2. Two way coupling

The two way coupling uses the following equations:

$$\boldsymbol{F}^s_{viscosity} + \boldsymbol{F}^s_{pressure} = \int_{\Gamma_{solid}} \boldsymbol{N}_i \boldsymbol{n} \cdot (\underline{\underline{\tau}}_{solid} + Ip) d\Gamma, \tag{11}$$

where the $\underline{\underline{\tau}}_{solid}$ is the stress term caused by viscosity; Γ_{solid} is the solid surface; $\boldsymbol{F}^s_{viscosity} = (\boldsymbol{F}^s_{viscosity,u}, \boldsymbol{F}^s_{viscosity,v}, \boldsymbol{F}^s_{viscosity,w})$ and has the form of:

$$\begin{aligned}
\boldsymbol{F}^s_{viscosity,u} &= \int_{V_{shell}} N_i(a_{xx}u_{sl} + a_{xy}v_{sl} + a_{xz}w_{sl})dV, \\
\boldsymbol{F}^s_{viscosity,v} &= \int_{V_{shell}} N_i(a_{yx}u_{sl} + a_{yy}v_{sl} + a_{yz}w_{sl})dV, \\
\boldsymbol{F}^s_{viscosity,w} &= \int_{V_{shell}} N_i(a_{zx}u_{sl} + a_{zy}v_{sl} + a_{zz}w_{sl})dV,
\end{aligned} \tag{12}$$

where V_{shell} denotes the mesh of a shell (a thin intermediate area between the solid and fluid [41]); μ is the viscosity coefficient; Δr is the thickness of the shell; $\mathbf{u}_{sl}$ is the slip velocity which is the velocity difference between the solid velocity $\mathbf{u}_s = (u_{s,u}, u_{s,v}, u_{s,w})$ and fluid velocity $\mathbf{u}_f = (u_{f,u}, u_{f,v}, u_{f,w})$, that is, $\mathbf{u}_{sl} = \mathbf{u}_s - \mathbf{u}_f$; and

$$\begin{aligned}
a_{xx} &= \frac{\mu}{\Delta r \Delta x_{wall}}(n_x(2 - \frac{2}{3})n_x + n_y n_y + n_z n_z), \\
a_{xy} &= \frac{\mu}{\Delta r \Delta x_{wall}}(-n_x\frac{2}{3}n_y + n_y n_x), \\
a_{xz} &= \frac{\mu}{\Delta r \Delta x_{wall}}(-n_x\frac{2}{3}n_z + n_z n_x), \\
a_{yx} &= \frac{\mu}{\Delta r \Delta x_{wall}}(n_x n_y - n_x\frac{2}{3}n_y), \\
a_{yy} &= \frac{\mu}{\Delta r \Delta x_{wall}}(n_x n_x + n_y(2 - \frac{2}{3})n_y + n_z n_z), \\
a_{yz} &= \frac{\mu}{\Delta r \Delta x_{wall}}(-n_y\frac{2}{3})n_z + n_z n_y), \\
a_{zx} &= \frac{\mu}{\Delta r \Delta x_{wall}}(n_x(n_z - n_z\frac{2}{3}n_x), \\
a_{zy} &= \frac{\mu}{\Delta r \Delta x_{wall}}(n_y n_z - n_z\frac{2}{3}n_y), \\
a_{zz} &= \frac{\mu}{\Delta r \Delta x_{wall}}(n_x n_x + n_y n_y + n_z(2 - \frac{2}{3})n_z).
\end{aligned}$$

Once obtaining $\boldsymbol{F}^s_{viscosity}$ and $\boldsymbol{F}^s_{pressure}$, the velocity of the solid $\boldsymbol{u}_s$=(u_s, v_s, w_s) can be calculated by equation (3). The the source term in (2) can then be obtained by [42]:

$$\begin{aligned}
\boldsymbol{s}^f_{c,x} &= a_{xx}u_s + a_{xy}v_s + a_{xz}w_s, \\
\boldsymbol{s}^f_{c,y} &= a_{yx}u_s + a_{yy}v_s + a_{yz}w_s, \\
\boldsymbol{s}^f_{c,z} &= a_{zx}u_s + a_{zy}v_s + a_{zz}w_s.
\end{aligned} \tag{13}$$

3. Construction of FSI NIROM using POD-RBF

In this section, the method of constructing NIROM for FSI problems using POD-RBF is described. The essence of this method lies in how to construct a set of interpolation functions or hyper surfaces that represent the reduced FSI system using POD-RBF non-intrusive reduced order modelling method [39]. Table 1 lists the variables used in the formulation below.

Variable	Definition
$\mathbf{u}^{POD}$	POD coefficients of coupled velocity components.
p^{POD}	POD coefficients of coupled pressure components.
v^{POD}	POD coefficients of coupled volume fraction components.
$\mathbf{u}$	Coupled velocity on full space.
p	Coupled pressure on full space.
v	Volume fraction on full space.
$\overline{\mathbf{u}}$	Mean of coupled velocities over the simulation period.
$\overline{v}$	Mean of coupled volumes fraction over the simulation period.
$\overline{p}$	Mean of coupled pressures over the simulation period.
$f_{\mathbf{u}}$	Hyper surface for the coupled velocity.
f_p	Hyper surface for the coupled pressure.
f_v	Hyper surface for the volume fraction .
ϕ	General radial basis functions.
$\Phi_{\mathbf{u}}$	POD basis functions of coupled velocity components.
Φ_p	POD basis functions of coupled pressure components.
Φ_v	POD basis functions of coupled volume fraction components.
N	Number of time steps.
M	Number of POD basis functions.

Table 1: Variables and definitions.

The POD method is used to form a set of POD basis functions from the snapshots which are the solutions to the high fidelity model recorded in time. The POD basis functions are optimal in the sense that they capture the most energy from the snapshots. This is achieved by performing the singular value decomposition (SVD) of the snapshots matrix A, that is, $A = E\Sigma F^T$ (E and F being orthogonal matrices, Σ being a diagonal matrix containing singular values arranged in a descending order). Then the POD basis functions Φ_i are the column of E, that is, $\Phi_j = E_{:,j}$, for $j \in \{1, 2 \dots m\}$. The solution of variables (velocity $\mathbf{u}$ for example) can be then expressed by a linear combination of the POD basis functions, $\mathbf{u} = \overline{\mathbf{u}} + \sum_{j=1}^{M} \Phi \mathbf{u}_j^{POD}$($\mathbf{u}^{POD}$ being POD coefficients). For additional details of the POD theory, see [43].

The RBF interpolation method is used here to obtain the POD coefficients. The RBF interpolation method builds up a interpolation function $f_i(x)$ using a summation of N RBFs, each associated with a center $\mathbf{C}$ and weighted by an weighting coefficient w_i, that is, $f_i(x) = \sum_{i=1}^{N} w_i * \phi(\|\mathbf{x} - \mathbf{C}\|)$. A RBF is a function whose value rely on the distance from a center point $\mathbf{C}$, so that $\phi(x) = \phi(\|x - \mathbf{C}\|)$. The norm is commonly chosen as the Euclidean distance. Commonly used types of radial basis functions are

multi-quadric, inverse quadratic, polyharmonic spline and Gaussian [39]. In this work, the Gaussian RBF is chosen to construct the approximate function. For additional details of the RBF interpolation theory, see [44].

The hyper surfaces of a FSI NIROM system which are used to calculate the POD coefficients have the following formulations:

$$\begin{aligned}
\mathbf{u}_j^{POD,n} &= f_{\mathbf{u},j}(\mathbf{u}^{POD,n-1}, p^{POD,n-1}, v^{POD,n-1}) = \sum_{i=1}^{N} w_{i,j} * \phi(r), \\
p_j^{POD,n} &= f_{p,j}(\mathbf{u}^{POD,n-1}, p^{POD,n-1}, v^{POD,n-1}) = \sum_{i=1}^{N} w_{i,j} * \phi(r), \\
v_j^{POD,n} &= f_{v,j}(\mathbf{u}^{POD,n-1}, p^{POD,n-1}, v^{POD,n-1}) = \sum_{i=1}^{N} w_{i,j} * \phi(r),
\end{aligned} \tag{14}$$

where $\mathbf{u}_j^{POD,n}, p_j^{POD,n}, v_j^{POD,n}$ are the POD coefficients of the coupled velocity, coupled pressure and volume fraction respectively (in which the subscript j denotes the j^{th} POD coefficient $j \in \{1, 2 \ldots m$ and the superscript n denotes the time step); $f_{\mathbf{u},j}, f_{p,j}, f_{v,j}$ denote the hyper surfaces that represents the reduced FSI system; $w_{i,j}$ is the weight of radial basis functions; $\phi(r)$ is the radial basis function. In this work, the Gaussian radial basis function is chosen:

$$\phi(r) = e^{-(r/\sigma)^2} = e^{-((\left\|(\mathbf{u}^{POD,n-1}, p^{POD,n-1}, v^{POD,n-1}) - \mathbf{C}\right\|)/\sigma)^2}, \tag{15}$$

where r is a radius and $\sigma > 0$ is the shape parameter; and $\left\|(\mathbf{u}_j^{POD,n-1}, p^{POD,n-1}, v^{POD,n-1}) - \mathbf{C}\right\|$ is a scalar distance from a given center $\mathbf{C}$ defined by the L2 norm. The center $\mathbf{C}$ is chosen to be the origin of the input data. The weights $w_{i,j}$ are to be determined to ensure the hyper surface $f_{u,j}, f_{p,j}, f_{v,j}$ match the given data. The weight is obtained by solving the equation:

$$A\mathbf{w}_{i,j} = y, \tag{16}$$

where A is matrix associated with the radius and $A_{k,l} = \phi(\left\|(u_k^{POD}, p_k^{POD}, v_k^{POD}) - \mathbf{C}\right\|)$, $k, l \in \{1, 2, \ldots, N\}$, N is the number of data points. $y = \mathbf{u}^{POD,n}, p^{POD,n}, v^{POD,n}$ is a vector containing the POD coefficients one time step after input POD coefficients.

The FSI NIROM algorithms consist of both offline and online processes and can be described as follows:

Algorithm 1: Offline algorithm for forming FSI NIROM using POD-RBF

(1) Generate several snapshots over the time period $[0, T]$ by solving the full couple system;

(2) Form a number of POD basis functions $\Phi_{\mathbf{u}}$, Φ_p and Φ_v through POD method;

(3) Obtain the functional values y at the data point $\mathbf{u}^{POD,t}$, $p^{POD,t}$, $v^{POD,t}$ through the solution from the full models, where $t \in \{1, 2, \ldots T\}$;

(4) Calculate the weights $\mathbf{w}_{i,j}$ by solving (16);

(5) Obtain a set of hyper surfaces by substituting the weight values obtained in above step into equation (14);

The online algorithm 2 described below will be used for calculation of the values of coupled velocity $\mathbf{u}$, coupled pressure p and volume fraction v.

Algorithm 2: Online calculation of the POD coefficients for FSI NIROM

(1) Initialize $\mathbf{u}_j^{POD,0}$, $p_j^{POD,0}$ and $v_j^{POD,0}$;

(2) Calculate solutions at current time step using following loop:

for $n = 1$ *to* N **do**
  for $j = 1$ *to* M **do**
    Solving fluid process:

(i) Assign a complete set of POD coefficients $u^{POD,n-1}$, $p^{POD,n-1}$ and $v^{POD,n-1}$ at previous time step $n-1$ to equation:

$$\begin{aligned} f_{\mathbf{u},j} &\leftarrow (\mathbf{u}^{POD,n-1}, p^{POD,n-1}, v^{POD,n-1}), \\ f_{p,j} &\leftarrow (\mathbf{u}^{POD,n-1}, p^{POD,n-1}, v^{POD,n-1}), \\ f_{v,j} &\leftarrow (\mathbf{u}^{POD,n-1}, p^{POD,n-1}, v^{POD,n-1}), \end{aligned}$$

(ii) Calculate the POD coefficient $u^{POD,n}$, $p^{POD,n}$ and $v^{POD,n}$ at current time step n using the following equations:

$$\begin{aligned} \mathbf{u}_j^{POD,n} &= f_{\mathbf{u},j} = \sum_{i=1}^{N} w_{i,j} * \phi_{\mathbf{u}}(r), \\ p_j^{POD,n} &= f_{p,j} = \sum_{i=1}^{N} w_{i,j} * \phi_{p}(r), \\ v_j^{POD,n} &= f_{v,j} = \sum_{i=1}^{N} w_{i,j} * \phi_{v}(r), \end{aligned}$$

  endfor
  Obtain the solution $\mathbf{u}^n$, p^n and v^n on full space at current time step n by projecting $\mathbf{u}_j^{POD,n}$, $p_j^{POD,n}$ and $v_j^{POD,n}$ onto the full space.

$$\mathbf{u}^n = \overline{\mathbf{u}} + \sum_{i=1}^{M} \Phi_{\mathbf{u}} u_i^{POD,n}, \quad p^n = \overline{p} + \sum_{i=1}^{M} \Phi_p p_i^{POD,n}, \quad v^n = \overline{v} + \sum_{i=1}^{M} \Phi_v v_i^{POD,n},$$

  Solving solid-fluid coupling:
  If (one way coupling) then
    $\boldsymbol{F}^s_{pressure} = \int_{\Gamma_{solid}} N_i n \cdot (Ip) d\Gamma, \quad \boldsymbol{s}_c^f = (\boldsymbol{s}_{c,x}^f, \boldsymbol{s}_{c,y}^f, \boldsymbol{s}_{c,z}^f)^T = 0.$
  Else If (two way coupling)
    $\boldsymbol{F}^s_{viscosity} + \boldsymbol{F}^s_{pressure} = \int_{\Gamma_{solid}} N_i n \cdot (\underline{\tau}_{solid} + Ip) d\Gamma,$
    obtain $\boldsymbol{s}_c^f = (\boldsymbol{s}_{c,x}^f, \boldsymbol{s}_{c,y}^f, \boldsymbol{s}_{c,z}^f)^T$ using equation (13).
  End If
endfor

4. Illustrative numerical examples

The FSI NIROM has been implemented under the framework of a combined finite-discrete element solid model (Y2D) and an advanced 3D unstructured mesh multi-phase fluid model (Fluidity).

The solid model, Y2D, uses a finite-strain formulation to solve the structural dynamics equations and is capable of modelling fracture network with any stiffness and shapes, vibration modes and stresses [45, 46, 47, 48]. It is coupled with the fluid multi-phase model Fluidity [49] to solve the fluid and solid coupling problem.

The fluid model, Fluidity, is capable of solving the Navier-Stoke equations and accompanying field equations on unstructured 1D, 2D and 3D finite element meshes. In order to obtain more accurate and stable solution from the high fidelity full model, a $P1_{DG}P2$ element pair is used in this work to accurately represent velocity and pressure changes between heterogeneous domains. The discontinuous Galerkin method is used for velocity while the continuous Galerkin method is used for pressure. One advantage of this FE pair is the mass matrix for velocity is a block diagonal matrix so that it can be trivially inverted. Another advantage is that it allows the order of the pressure to be increased to quadratic whilst maintaining Ladezinskya-Babuska-Brezzi (LBB) stability [50]. This element also has the ability represent very accurately the balance between the pressure or free surface gradients and the Coriolis force as well as buoyancy forces.

4.1. Case 1: one way coupling test case - flow past a cylinder

The first case for numerical illustration of the method proposed in this paper is a one-way coupling test case: flow past a solid cylinder case. This problem domain consists of a rectangle of non-dimensional size 2.2×0.41 and the radius of the solid cylinder is 0.05.

The problem was discretised with a mesh of 20058 nodes during the simulation time period $[0, 4]$ with a time step size of $\Delta t = 0.001$ which ensures the Courant number is smaller than 0.5. 100 snapshots were taken from the pre-computed solutions at regularly spaced time intervals 0.04 and a number of POD bases were generated for variables $\mathbf{u}$, p, v through these snapshots.

Figure 1 shows the singular eigenvalues in order of decreasing magnitude. In general, the more POD bases are chosen, the more energy can be captured. In this case, as shown in figure 1, the singular eigenvalues decrease satisfying the Kolmogorov criterion drastically in the first 2 leading singular eigenvalues, which means the first 2 POD bases captured most energy (79.28%). This figure provides a criterion for choosing the number of POD bases.

Figure 2 shows the velocity solutions at time instances $t = 2.0$ and $t = 3.2$, as calculated using the high fidelity full model and FSI NIROM with 3, 6 and 20 POD bases. It can be seen that the FSI NIROM attains closer agreement to the full model as more POD bases are chosen. The FSI NIROM has captured 82.90%, 90.99%, 98.35% of energy in fluid dynamics using 3, 6 and 20 POD bases respectively in this example.

Figure 3 shows the error in velocity solutions predicted by the FSI NIROM using 3, 6 and 20 POD bases at time instances 2.0 and 3.2. The error in velocity solutions is decreased by 80% when the number of POD bases is increased from 3 to 20. The FSI

NIROM with 20 POD bases exhibits an overall good agreement with the high fidelity full model.

To further assess the accuracy of the FSI NIROM, the velocity solution at a particular point ($x = 0.27543, y = 0.29336$) is displayed in figure 4. Again shown in this figure, an increase in the number of POD bases results in improved accuracy, which is consistent with the results shown in figure 2 and 3.

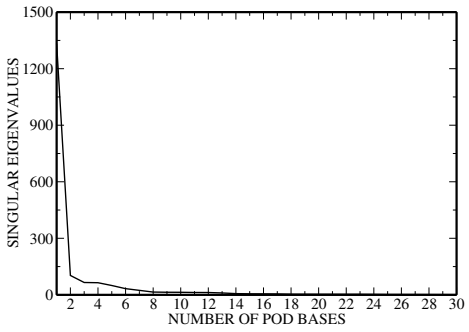

Figure 1: Case 1 (flow past a cylinder): the figure shows the singular eigenvalues in order of decreasing magnitude.

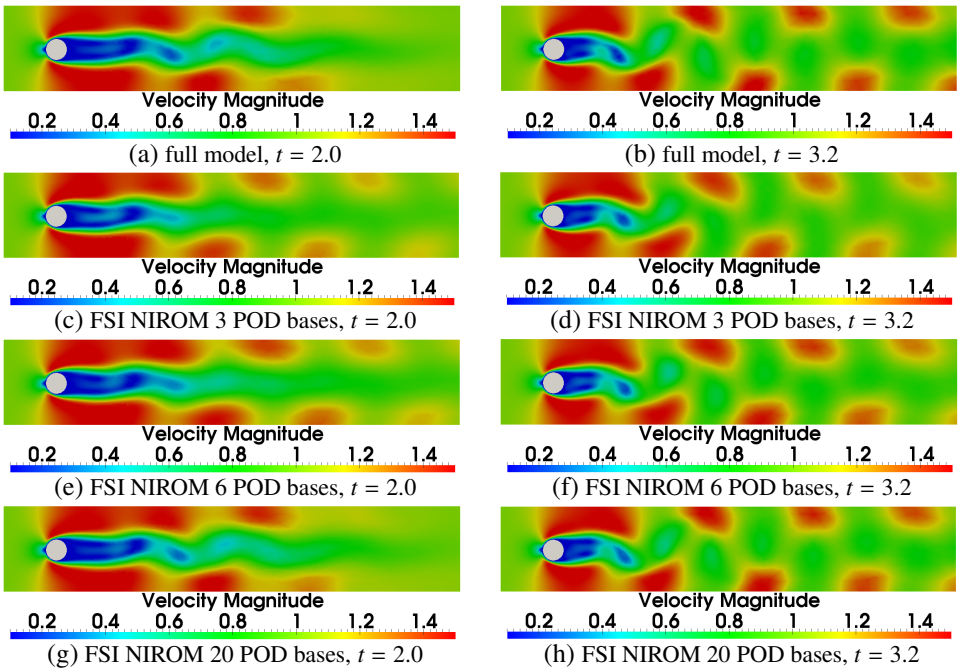

(a) full model, $t = 2.0$ (b) full model, $t = 3.2$

(c) FSI NIROM 3 POD bases, $t = 2.0$ (d) FSI NIROM 3 POD bases, $t = 3.2$

(e) FSI NIROM 6 POD bases, $t = 2.0$ (f) FSI NIROM 6 POD bases, $t = 3.2$

(g) FSI NIROM 20 POD bases, $t = 2.0$ (h) FSI NIROM 20 POD bases, $t = 3.2$

Figure 2: Case 1 (flow past a cylinder): the figures displayed above show the velocity solutions at time instances 2.0 (left panel) and 3.2 (right panel). In NIROM, 3, 6 and 20 POD bases are chosen with 100 snapshots).

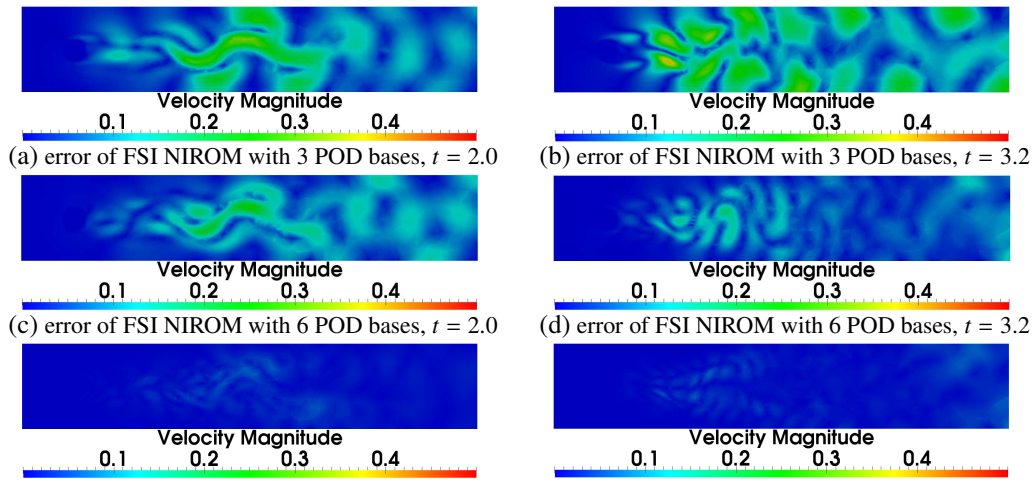

(a) error of FSI NIROM with 3 POD bases, $t = 2.0$ (b) error of FSI NIROM with 3 POD bases, $t = 3.2$

(c) error of FSI NIROM with 6 POD bases, $t = 2.0$ (d) error of FSI NIROM with 6 POD bases, $t = 3.2$

(e) error of FSI NIROM with 20 POD bases, $t = 2.0$ (f) error of FSI NIROM with 20 POD bases, $t = 3.2$

Figure 3: Case 1 (flow past a cylinder): the figures displayed above show the solution difference between the full model and the FSI NIROM using 3, 6 and 20 POD bases at time instances 2.0 (left panel) and 3.2 (right panel).

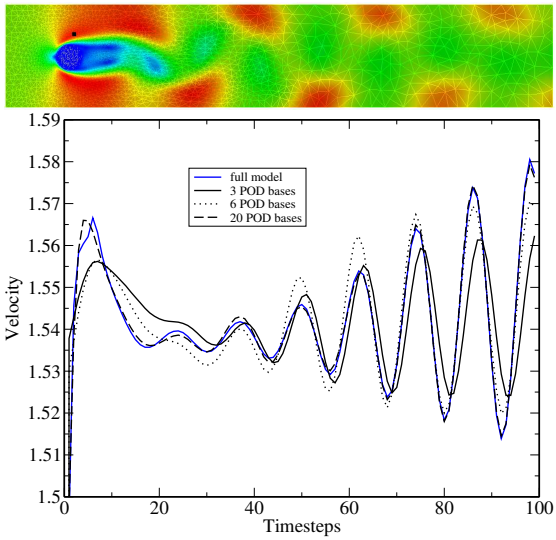

Figure 4: case 1 (flow past a cylinder): velocity solution from high fidelity model and FSI NIROM using 3, 6 and 20 POD bases at point (x=0.27543, y=0.29336)

4.2. Case 2:two-way coupling case - a 2D free-falling square in water

The second illustrative case is a 2D free-falling case, that is, a square that falls through a vertical domain is subjected to the gravitational force. The domain has a non-dimensional size of 2.5×10 and the size of the solid square is 0.25×0.25. The number of nodes on the mesh is 93000. The length of the simulation time period is 2.5 s. The time step is set to 0.01 s which ensures the Courant number is smaller than 0.5. 250 snapshots were recorded at each time step.

Figure 5 shows the singular eigenvalues in order of decreasing magnitude. Figure 6 shows the first 72 POD bases. It can be seen that most of flow features are captured within the first 12 leading POD bases while the small-scale flow features are represented by the 36^{th} - 72^{th} POD bases. The first few POD bases are capable of capturing most of the energy. In this work, 12, 36 and 72 POD bases are chosen to illustrate how to improve the accuracy of results by increasing the number of POD bases.

Figure 7 depicts the velocity solutions from the full model and NIROM at time instances $t = 1.0\ s$, $1.5\ s$, $2.0\ s$ and $2.5\ s$. It can be seen that the FSI NIROM performs well using 12 POD bases, better results are obtained by increasing the number of POD bases to 72, which captured almost 99% of the total energy. A comparison of the velocity fields generated by the high fidelity model and the FSI NIROMs with 12, 36 and 72 POD bases at a particular point $(x = 1.25, y = 7.84)$ in the computational domain are presented in figure 8.

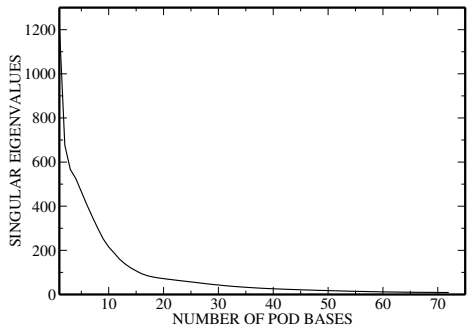

Figure 5: Case 2 (a 2D free-falling square in water): the figure shows the singular eigenvalues in order of decreasing magnitude.

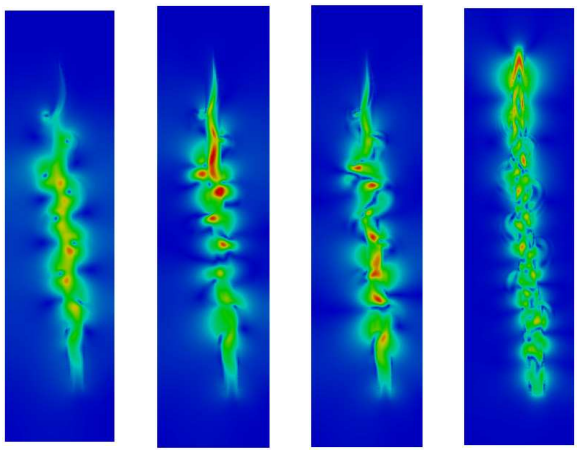

(a) 1st (b) 2nd (c) 3rd (d) 12th

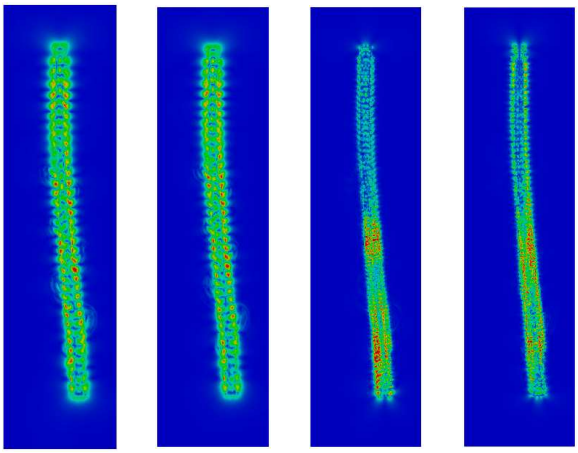

(a) 36th (b) 38th (c) 71st (d) 72th

Figure 6: Case 2 (a 2D free-falling square in water): the figures displayed above show the first, second, third, $12^{th}, 36^{th}, 38^{th}, 71^{th}$ and 72^{th} POD bases.

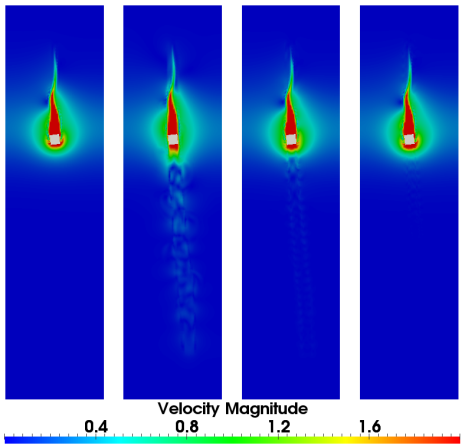

(a) full model, NIROM with 12, 36 and 72 POD, $t = 1.0$

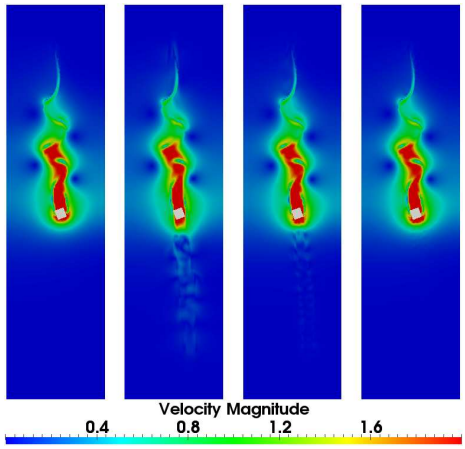

(b) full model, NIROM with 12, 36 and 72 POD, $t = 1.5$

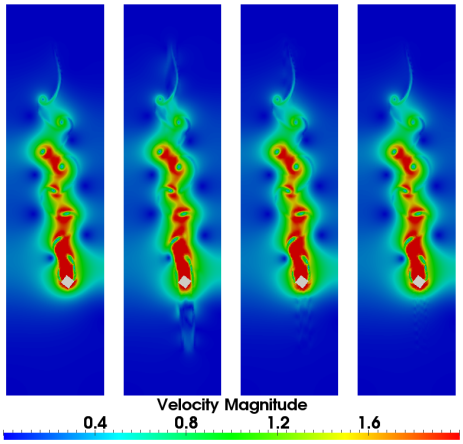

(c) full model, NIROM with 12, 36 and 72 POD, $t = 2.0$

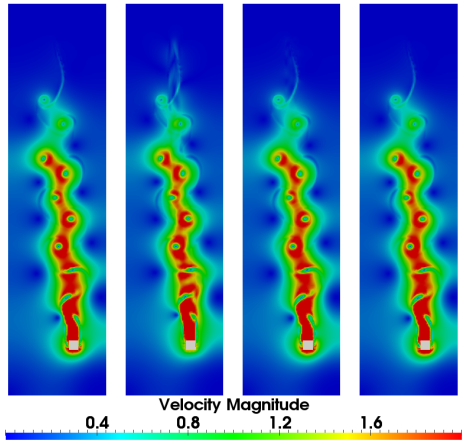

(d) full model, NIROM with 12, 36 and 72 POD, $t = 2.5$

Figure 7: Case 2 (a 2D free-falling square in water): the figures displayed above show the solutions from full model and NIROM using 12, 36 and 72 POD bases at $t = 1.0$ (top left panel), $t = 1.5$ (top right panel), $t = 2.0$ (bottom left panel) and $t = 2.5$ (bottom right panel). In each panel, from left to right, full model, NIROM with 12, 36 and 72 POD basis functions, respectively.

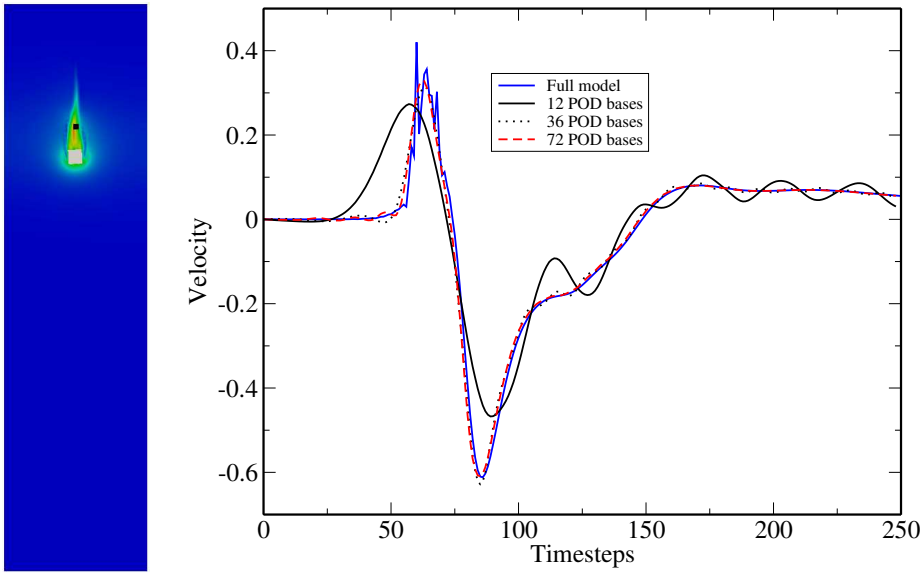

(a) location (b) velocity solutions comparison at a particular point (x=1.25, y=7.84).

Figure 8: Case 2 (a 2D free-falling square in water): a comparison of the velocity fields generated by the high fidelity model and the FSI NIROMs with 12, 36 and 73 POD bases at a particular point (x=1.25, y=7.84), as shown in (a).

4.3. Case 3: Vortex-induced vibrations of an elastic beam

The third case is the vortex-induced vibrations of an elastic beam embedded in fluids. The computational domain is presented in figure 9 which has an elastic solid beam with a density of 100 enclosed within a rectangle computational domain. The rectangle computational domain has a non-dimensional size of 6×2. The elastic beam with a density of 100 has a size of 1×0.286 and is located on the bottom in the middle of the rectangle. A slip boundary condition is applied to the top, bottom and left sides, an open boundary condition applied to the right side. The inlet velocity at the left side is set to 20. The simulation period is $[0, 0.5]$ with a time step size of $\Delta t = 0.001$ which ensures the Courant number is smaller than 0.5.

The vortex-induced vibration problem was solved using an unstructured mesh of 28800 nodes illustrated in figure 9. 100 snapshots were taken at a regularly spaced time intervals 0.005. From these snapshots, a number of POD bases were generated.

Figure 10 presents the velocity solutions obtained from the high fidelity model and FSI NIROM with 6, 12 and 50 POD bases at time instances $t = 0.15$ and $t = 0.5$. It illustrates that the solutions from FSI NIROM are in close agreement with the high fidelity full model. It can be seen from the figure that only 6 POD bases already captured the velocity profiles well. The complex flow patterns are captured very well by using a larger number of POD bases − as shown in figures 10(g) and 10(h). It is also shown that the solution of FSI NIROM is closer to that of high fidelity full model as the number of POD bases is increased. This is illustrated by figure 11 which shows the error of velocity solutions predicted by the FSI NIROM with 6, 12 and 50 POD bases at time instances $t = 0.15$ and $t = 0.5$. It is evident that FSI NIROM with a larger number of POD bases exhibits less error.

Figure 12 presents the pressure profiles obtained from the high fidelity model and FSI NIROM with 6, 12 and 50 POD bases at time instances $t = 0.15$ and $t = 0.5$. It is shown that the FSI NIROM with 50 POD bases is in closer agreement with the high fidelity full model. In order to investigate the difference between the high fidelity model and FSI NIROM, the pressure solutions at a particular point $(x = 2, y = 1.05)$ in the computational domain are presented in figure 13. The figure shows that FSI NIROM with 12 and 50 POD bases exhibits a very good agreement with the high fidelity full model.

To validate the accuracy of FSI NIROM, the correlation coefficients, root mean squared error (RMSE) and normalized root mean square error (NRMSE) of pressure solutions are provided in figure 14. In this work, the RMSE and NRMSE are used to measure the pressure differences between the high fidelity model and NIROM at all nodes for every time level, which are calculated below:

$$RMSE^n = \sqrt{\frac{\sum_{i=1}^{\mathcal{N}} (P^n_{full,i} - P^n_{rom,i})^2}{\mathcal{N}}}, \quad NRMSE^n = \frac{RMSE^n}{P^n_{max} - P^n_{min}}, \tag{17}$$

where n is the time level; $\mathcal{N}$ denotes the number of nodes; $P_{full,i}$ and $P_{rom,i}$ are pressure solutions from the high fidelity full model and NIROM at the node number i respectively; P^n_{max} and P^n_{min} are the maximum and minimum values of pressure solutions over the computational domain at time level n. It is seen that the FSI NIROM performs

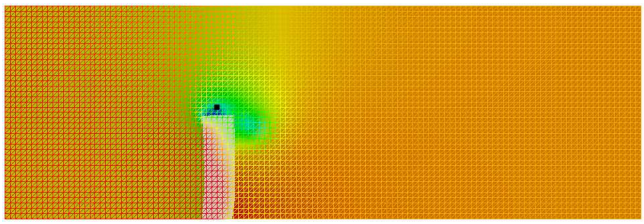

Figure 9: Case 3 (vortex-induced vibrations): a comparison of pressure solutions between the high fidelity model and FSI NIROM at a particular point(x=2, y=1.05).

better when using a larger number of POD bases. Using 50 POD bases, most of the NRMSE is smaller than 0.025 during the computational period and the errors in pressure solutions are decreased by $30\% - 50\%$ in comparison to that using 6 POD bases.

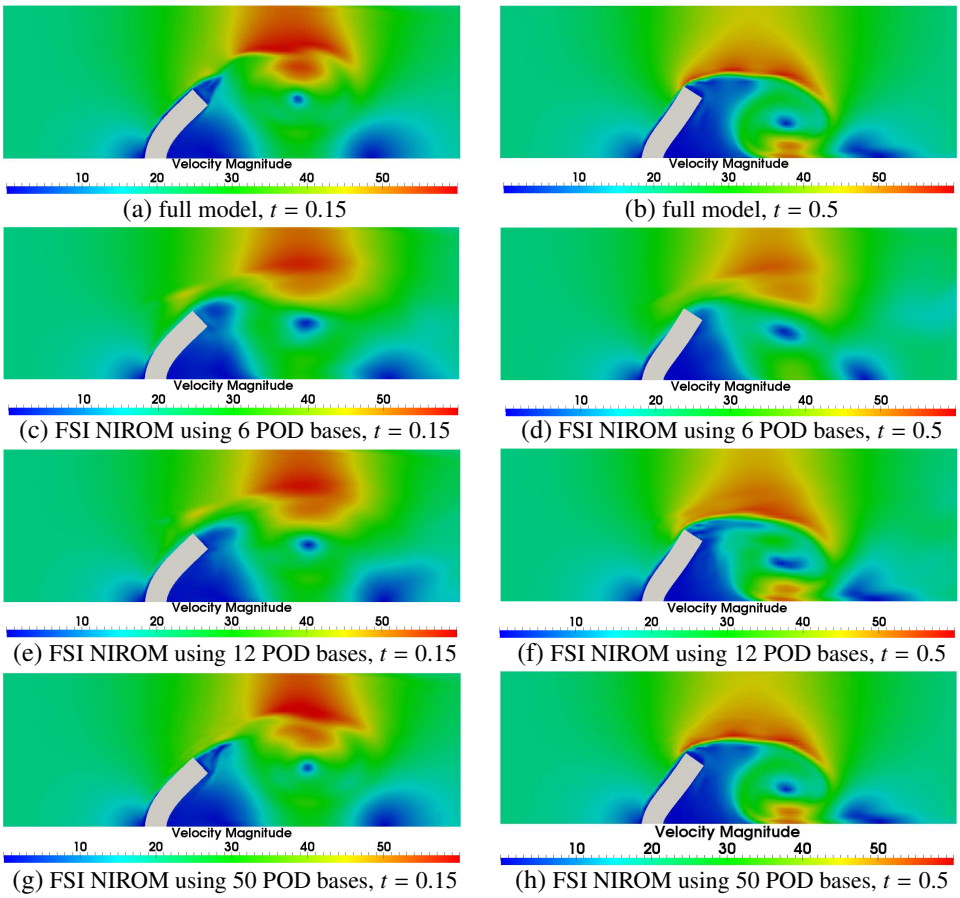

(a) full model, $t = 0.15$ (b) full model, $t = 0.5$

(c) FSI NIROM using 6 POD bases, $t = 0.15$ (d) FSI NIROM using 6 POD bases, $t = 0.5$

(e) FSI NIROM using 12 POD bases, $t = 0.15$ (f) FSI NIROM using 12 POD bases, $t = 0.5$

(g) FSI NIROM using 50 POD bases, $t = 0.15$ (h) FSI NIROM using 50 POD bases, $t = 0.5$

Figure 10: Case 3 (vortex-induced vibrations): a comparison of velocity solutions between the high fidelity model and FSI NIROM with 6, 12 and 50 POD bases at time instances $t = 0.15$ (left panel) and $t = 0.5$ (right panel).

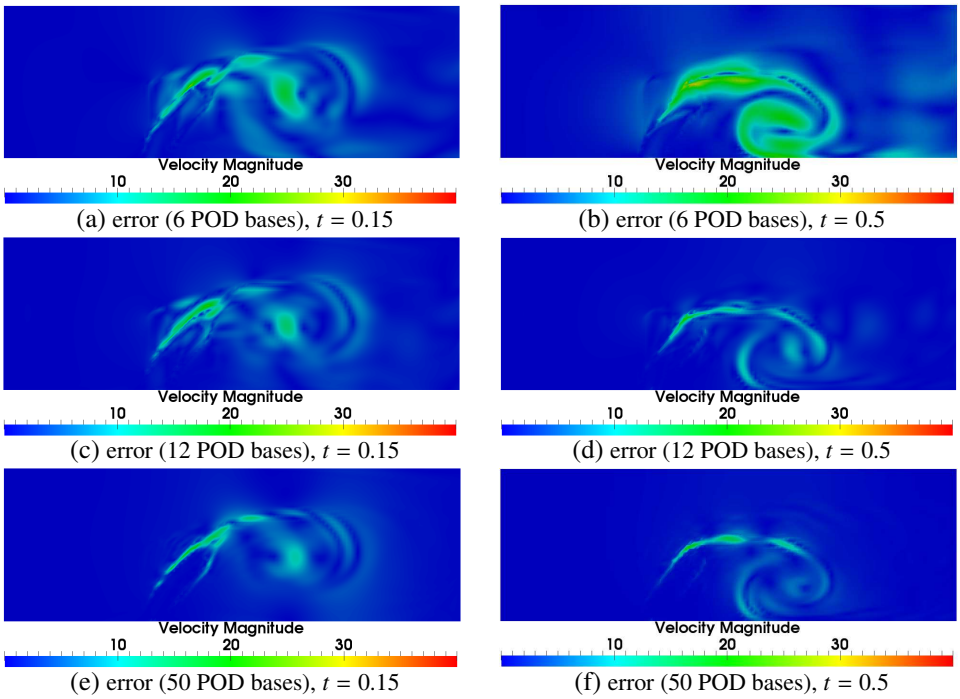

(a) error (6 POD bases), $t = 0.15$ (b) error (6 POD bases), $t = 0.5$

(c) error (12 POD bases), $t = 0.15$ (d) error (12 POD bases), $t = 0.5$

(e) error (50 POD bases), $t = 0.15$ (f) error (50 POD bases), $t = 0.5$

Figure 11: Case 3 (vortex-induced vibrations): error in velocity solutions obtained from FSI NIROM with 6, 12 and 50 POD bases at time instances $t = 0.15$ (left panel) and $t = 0.5$ (right panel).

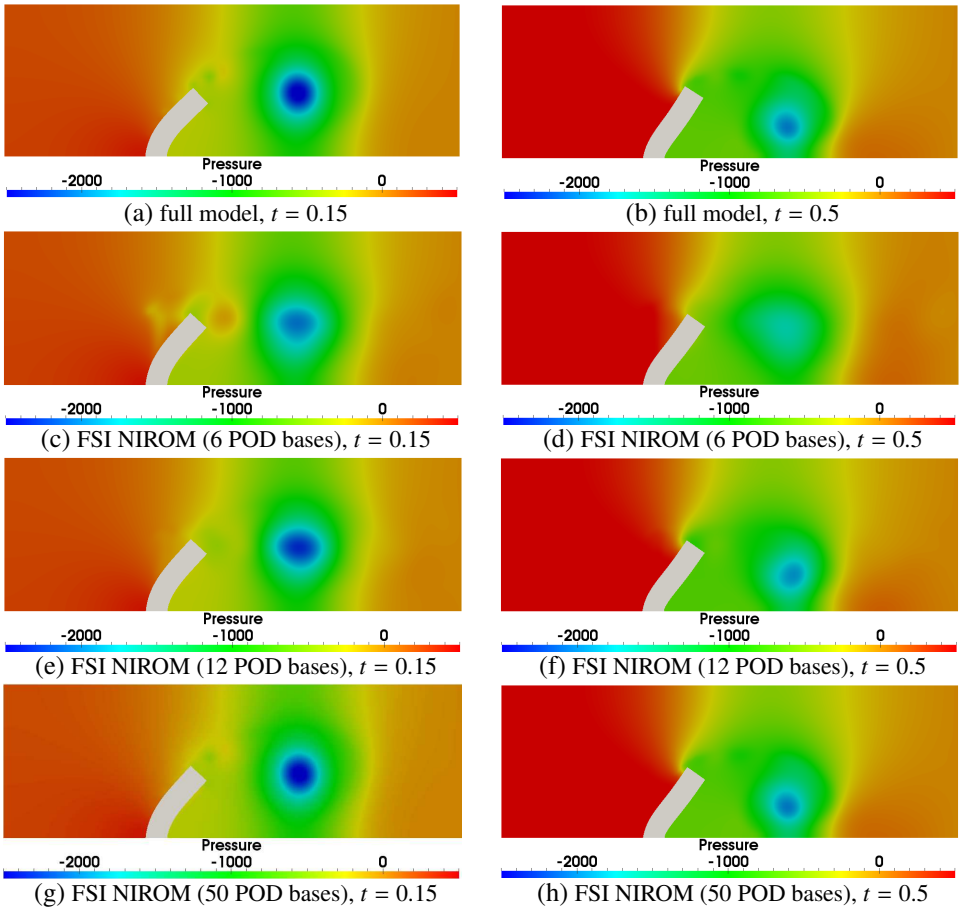

(a) full model, $t = 0.15$ (b) full model, $t = 0.5$

(c) FSI NIROM (6 POD bases), $t = 0.15$ (d) FSI NIROM (6 POD bases), $t = 0.5$

(e) FSI NIROM (12 POD bases), $t = 0.15$ (f) FSI NIROM (12 POD bases), $t = 0.5$

(g) FSI NIROM (50 POD bases), $t = 0.15$ (h) FSI NIROM (50 POD bases), $t = 0.5$

Figure 12: Case 3 (vortex-induced vibrations): a comparison of Pressure solutions between the high fidelity model and FSI NIROM with 6, 12 and 50 POD bases at time instances $t = 0.15$ (left panel) and $t = 0.5$ (right panel).

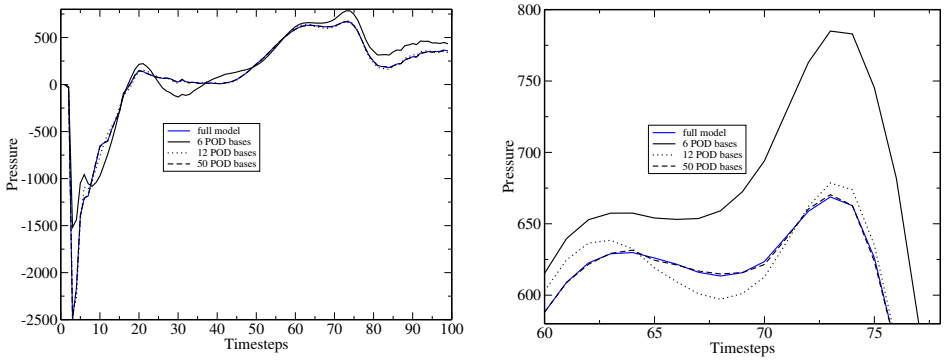

(a) pressure solution (b) blowup of the pressure solution in (a)

Figure 13: Case 3 (vortex-induced vibrations): a comparison of pressure solutions between the high fidelity model and FSI NIROM at a particular point(x=2, y=1.05).

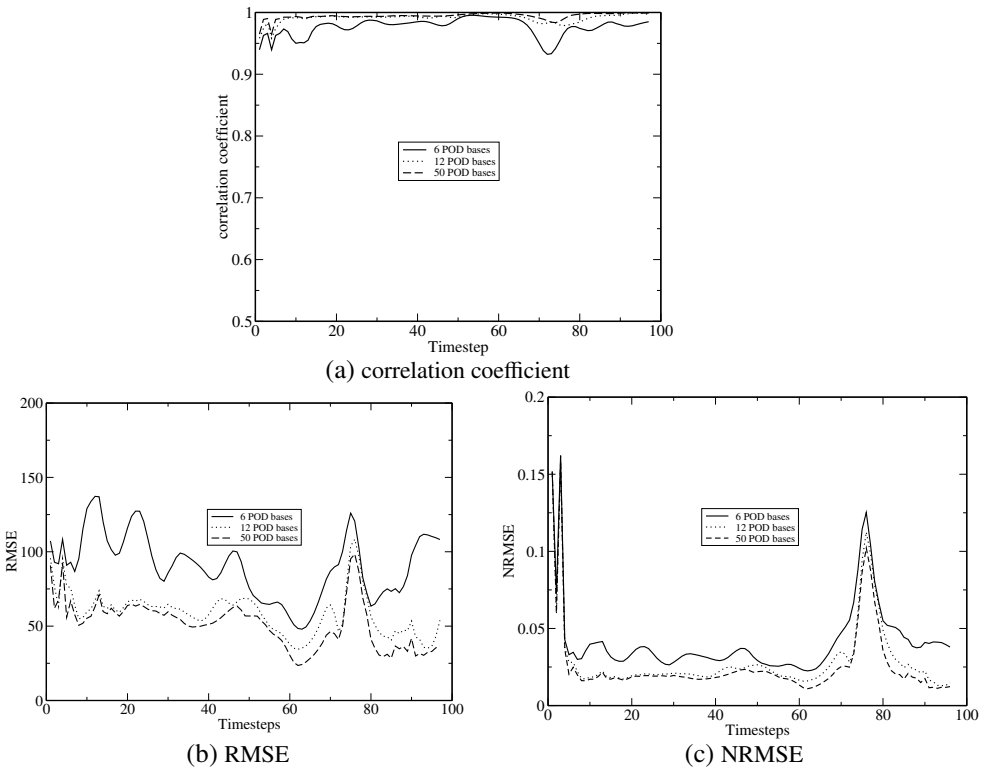

(a) correlation coefficient

(b) RMSE (c) NRMSE

Figure 14: Case 3 (vortex-induced vibrations): correlation coefficient, RMSE and NRMSE of pressure solutions between the high fidelity and FSI NIROM with 6, 12 and 50 POD bases.

4.4. Computational efficiency of the FSI NIROM

In this section, the computational cost required for running three test cases from the high fidelity full model and FSI NIROM is provided. The simulation workstation has 12 processors and a 48GB random-access memory(RAM). The processor used in workstation is Intel(R) Xeon(R) CPU X5680 @ 3.33GHz. In this work only one single processor with frequency of 3.33GHz was used since the test cases were performed in serial. Table 2 shows the online CPU time (seconds) required for running the full model and FSI NIROM ROM at one time step for three test cases. It can be seen that the computational cost of FSI NIROM required for the test cases is reduced significantly by 5-6 orders of magnitude. Only interpolating the POD coefficients and projecting the POD coefficients back onto the full space are involved in the online calculation of FSI NIROM. In addition, the FSI NIROM is expected to gain more CPU savings if a finer mesh is used.

Table 2: Online CPU time (seconds) required for running the full model and FSI NIROM during one snapshot for three cases (one snapshots includes forty time-steps for case 1, one time-step for case 2 and five time-steps for case 3.

Cases	Model	Assembling and Solving	Projection	Interpolation	Total
Flow past a cylinder	Full model	290.6667	0	0	290.6667
	FSI NIROM	0	0.0003	0.0001	0.00040
Free-falling square	Full model	29.2786	0	0	29.2786
	FSI NIROM	0	0.0003	0.0001	0.00040
Bending beam	Full model	102.6269	0	0	102.6269
	FSI NIROM	0	0.0003	0.0001	0.00040

The offline CPU cost includes the time required to form the POD bases and the interpolation functions. It is found that the time for calculating the interpolation functions can be ignored. Figure 15 illustrates the offline CPU time required to form the POD bases. The offline CPU time is dependent on the number of POD bases and nodes. It is seen that for a given number of nodes, the relationship between the offline CPU time and number of POD bases is linear. The offline CPU time increases with the increased number of POD bases. For a given number of nodes, the gradient of lines (representing the increased rate of CPU time when the number of POD bases increases) is 0.09 for cases 1 and 3 while 0.88 for case 2. In the three test cases, the offline CPU time required for the NIROM is $0.1\% - 7\%$ of that required for the full simulation when using the maximum number of POD bases.

5. Conclusion

A POD-RBF method has been, for the first time, used to construct a non-intrusive reduced order model for the fluid-structure interactions (FSI) problem and developed under the framework of the combined finite-discrete element method based solid model (Y2D) and unstructured mesh finite element multi-phase model (Fluidity). A RBF multi-dimensional interpolation method is used to construct a set of interpolated hyper

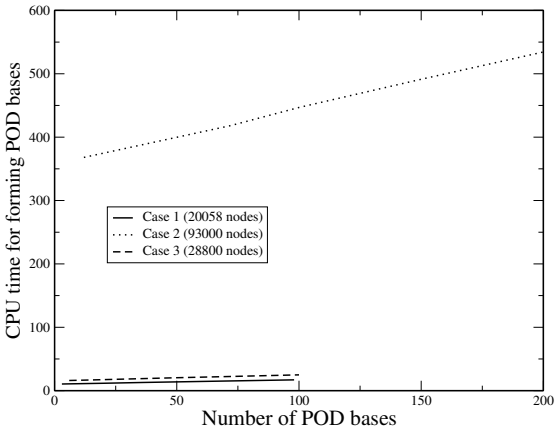

Figure 15: The offline CPU time required to form POD bases.

surfaces representing the reduced FSI system. Due to non-intrusiveness, the novel FSI NIROM for fluid-solid coupling modelling is independent of the original system and source code for fluid and solid simulations, therefore, it is easy to be extended to future developments and applications.

The performance of the novel FSI NIROM has been demonstrated by three test coupling cases: a one-way coupling case (flow past a cylinder), two two-way coupling cases (a free-falling cylinder in water and a vortex-induced vibrations of an elastic beam case). A detailed comparison between the high fidelity model and FSI NIROM has been carried out. An accuracy assessment has also been made for the FSI NIROM. The numerical simulations show that the FSI NIROM exhibits comprehensive good agreement with the high fidelity model. The results of FSI NIROM can be improved by choosing a larger number of POD bases. A significant CPU speed-up has been obtained by the FSI NIROM method and additional speed-up can be expected as the number of nodes is increased. Future work will investigate applying this model to more complex coupling problem such as blasting and parametric cases (variable material properties).

Acknowledgments

This work was carried out under funding from Janet Watson scholarship at Department of Earth Science and Engineering. Authors would like to acknowledge the support of the UK's Natural Environment Research Council projects(NER/A/S/2003/00595, NE/C52101X/1 and NE/C51829X/1), the Engineering and Physical Sciences Research Council (GR/R60898, EP/I00405X/1 and EP/J002011/1), and the Imperial College High Performance Computing Service. Prof. I.M. Navon acknowledges the support of NSF/CMG grant ATM-0931198. Dr. Xiao acknowledges the support of NSFC grant 11502241 and China postdoctoral science foundation grant (2014M562087). Prof. Pain and Dr. Fang are greatful for the support provided by BP. Prof. Pain is grateful for the support of the EPSRC MEMPHIS multi-phase flow programme grant. The research leading to these results has received funding from the European Union Seventh Frame-

work Programme (FP7/20072013) under grant agreement No.603663 for the research project PEARL (Preparing for Extreme And Rare events in coastal regions).

References

[1] Hans-Joachim Bungartz and Michael Schäfer. *Fluid-structure interaction: modelling, simulation, optimisation*, volume 1. Springer Science & Business Media, 2006.

[2] F.Fang, C.Pain, I.M. Navon, A.H. Elsheikh, J. Du, and D.Xiao. Non-linear Petrov-Galerkin methods for Reduced Order Hyperbolic Equations and Discontinuous Finite Element Methods. *Journal of Computational Physics*, 234:540–559, 2013.

[3] F Fang, T Zhang, D Pavlidis, C.C. Pain, AG Buchan, and I.M. Navon. Reduced order modelling of an unstructured mesh air pollution model and application in 2D/3D urban street canyons. *Atmospheric Environment*, 96:96–106, 2014.

[4] F Fang, C.C. Pain, I.M. Navon, GJ Gorman, MD Piggott, PA Allison, and AJH Goddard. A POD goal-oriented error measure for mesh optimization. *International Journal for Numerical Methods in Fluids*, 63(2):185–206, 2010.

[5] Matteo Diez, Emilio F Campana, and Frederick Stern. Design-space dimensionality reduction in shape optimization by karhunen–loève expansion. *Computer Methods in Applied Mechanics and Engineering*, 283:1525–1544, 2015.

[6] Manal Alotaibi, Victor M Calo, Yalchin Efendiev, Juan Galvis, and Mehdi Ghommem. Global–local nonlinear model reduction for flows in heterogeneous porous media. *Computer Methods in Applied Mechanics and Engineering*, 292:122–137, 2015.

[7] D. Xiao, F. Fang, C.C. Pain, I.M. Navon, P. Salinas, and A. Muggeridge. Non-intrusive reduced order modeling of multi-phase ow in porous media using the pod-rbf method. *submitted to Journal of Computational Physics*, 2015.

[8] Razvan Stefanescu and I.M. Navon. POD/DEIM nonlinear model order reduction of an adi implicit shallow water equations model. *Journal of Computational Physics*, 237:95–114, 2013.

[9] Razvan Stefanescu, Adrian Sandu, and I.M. Navon. Comparison of POD reduced order strategies for the nonlinear 2D shallow water equations. *International Journal for Numerical Methods in Fluids*, 76(8):497–521, 2014.

[10] D.N. Daescu and I.M. Navon. A dual-weighted approach to order reduction in 4d-var data assimilation. *Monthly Weather Review*, 136(3):1026–1041, 2008.

[11] Andrea Manzoni, Filippo Salmoiraghi, and Luca Heltai. Reduced basis isogeometric methods (rb-iga) for the real-time simulation of potential flows about parametrized naca airfoils. *Computer Methods in Applied Mechanics and Engineering*, 284:1147–1180, 2015.

[12] AG Buchan, AA Calloo, MG Goffin, S Dargaville, F Fang, CC Pain, and IM Navon. A pod reduced order model for resolving angular direction in neutron/photon transport problems. *Journal of Computational Physics*, 296:138–157, 2015.

[13] Răzvan Ştefănescu, Adrian Sandu, and Ionel Michael Navon. Pod/deim reduced-order strategies for efficient four dimensional variational data assimilation. *Journal of Computational Physics*, 295:569–595, 2015.

[14] Michael Schlegel and Bernd R. Noack. On long-term boundedness of galerkin models. *Journal of Fluid Mechanics*, 765:325–352, 2 2015.

[15] Jan sth, Bernd R. Noack, SiniÅa Krajnovi, Diogo Barros, and Jacques Bore. On the need for a nonlinear subscale turbulence term in pod models as exemplified for a high-reynolds-number flow over an ahmed body. *Journal of Fluid Mechanics*, 747:518–544, 5 2014.

[16] Leopoldo P. Franca and Sergio L. Frey. Stabilized finite element methods: Ii. the incompressible Navier-Stokes equations. *Computer Methods in Applied Mechanics and Engineering*, 99(2-3):209–233, 1992.

[17] S. Chaturantabut and D.C. Sorensen. Nonlinear model reduction via discrete empirical interpolation. *SIAM J. Sci. Comput*, 32:2737–2764, 2010.

[18] D. Xiao, F. Fang, J. Du, C.C. Pain, I.M. Navon, A. G. Buchan, A.H. ElSheikh, and G. Hu. Non-linear Petrov-Galerkin methods for reduced order modelling of the Navier-Stokes equations using a mixed finite element pair. *Computer Methods In Applied Mechanics and Engineering*, 255:147–157, 2013.

[19] C. Bou-Mosleh K. Carlberg and C. Farhat. Efficient non-linear model reduction via a least-squares Petrov-Galerkin projection and compressive tensor approximations. *International Journal for Numerical Methods in Engineering*, 86:155–181, 2011.

[20] M. Serpas Y. Chu and J. Hahn. State-preserving nonlinear model reduction procedure. *Chemical Engineering Science*, 66:3907–3913, 2011.

[21] Alireza Jafarpour Feriedoun Sabetghadam. α Regularization of the POD-Galerkin dynamical systems of the Kuramoto-Sivashinsky equation. *Applied Mathematics and Computation*, 218:6012–6026, 2012.

[22] Karen Willcox and Alexandre Megretski. Model reduction for large-scale linear applications. In *Proc. of 13th IFAC Symposium on System Identification, Rotterdam, Netherlands*, pages 1431–1436, 2003.

[23] M. Barrault, Y. Maday, N.C. Nguyen, and A.T. Patera. An empirical interpolation method: application to efficient reduced-basis discretization of partial differential equations. *C. R. Acad. Sci. Paris, Ser*, 339:667–672, 2004.

[24] D. Xiao, F. Fang, A. G. Buchan, C.C. Pain, I.M. Navon*, J. Du, , and G. Hu. Non-linear model reduction for the Navier-Stokes equations using Residual DEIM method. *Journal of Computational Physics*, 263:1–18, 2014.

[25] Kevin Carlberg, Charbel Farhat, Julien Cortial, and David Amsallem. The gnat method for nonlinear model reduction: effective implementation and application to computational fluid dynamics and turbulent flows. *Journal of Computational Physics*, 242:623–647, 2013.

[26] Juan Du, Fangxin Fang, Christopher C Pain, I.M. Navon, Jiang Zhu, and David A Ham. POD reduced-order unstructured mesh modeling applied to 2d and 3d fluid flow. *Computers and Mathematics with Applications*, 65(3):362–379, 2013.

[27] F. Fang, C.C. Pain, I.M. Navon, M.D. Piggott, G.J. Gorman, P.A. Allison, and A.J.H. Goddard. Reduced-order modelling of an adaptive mesh ocean model. *International journal for numerical methods in fluids*, 59(8):827–851, 2009.

[28] Matthew F Barone, Irina Kalashnikova, Matthew R Brake, and Daniel J Segalman. Reduced order modeling of fluid/structure interaction. *Sandia National Laboratories Report, SAND No*, 7189, 2009.

[29] I Kalashnikova, MF Barone, and MR Brake. A stable Galerkin reduced order model for coupled fluid–structure interaction problems. *International Journal for Numerical Methods in Engineering*, 95(2):121–144, 2013.

[30] T Lieu, C Farhat, and M Lesoinne. Reduced-order fluid/structure modeling of a complete aircraft configuration. *Computer methods in applied mechanics and engineering*, 195(41):5730–5742, 2006.

[31] Thuan Lieu, Charbel Farhat, and Michel Lesoinne. Pod-based aeroelastic analysis of a complete f-16 configuration: Rom adaptation and demonstration. *AIAA Paper*, 2295:2005, 2005.

[32] Erwan Liberge, Marie Pomarede, and Aziz Hamdouni. Reduced-order modelling by pod-multiphase approach for fluid-structure interaction. *European Journal of Computational Mechanics/Revue Européenne de Mécanique Numérique*, 19(1-3):41–52, 2010.

[33] Davide Forti and Gianluigi Rozza. Efficient geometrical parametrisation techniques of interfaces for reduced-order modelling: application to fluid–structure interaction coupling problems. *International Journal of Computational Fluid Dynamics*, 28(3-4):158–169, 2014.

[34] Chen Han. Blackbox stencil interpolation method for model reduction. Master's thesis, Massachusetts Institute of Technology, 2012.

[35] D. Xiao, F. Fang, A.G. Buchan, C.C. Pain, I.M. Navon, and A. Muggeridge. Non-intrusive reduced order modelling of the Navier–Stokes equations. *Computer Methods in Applied Mechanics and Engineering*, 293:552–541, 2015.

[36] S Walton, O Hassan, and K Morgan. Reduced order modelling for unsteady fluid flow using proper orthogonal decomposition and radial basis functions. *Applied Mathematical Modelling*, 37(20):8930–8945, 2013.

[37] Christophe Audouze, Florian De Vuyst, and Prasanth B Nair. Nonintrusive reduced-order modeling of parametrized time-dependent partial differential equations. *Numerical Methods for Partial Differential Equations*, 29(5):1587–1628, 2013.

[38] C Audouze, F De Vuyst, and PB Nair. Reduced-order modeling of parameterized PDEs using time–space-parameter principal component analysis. *International journal for numerical methods in engineering*, 80(8):1025–1057, 2009.

[39] D. Xiao, F. Fang, C. Pain, and G. Hu. Non-intrusive reduced order modelling of the Navier-Stokes equations based on RBF interpolation. *International Journal for Numerical Methods in Fluids*, 79(11):580–595, 2015.

[40] Ante Munjiza. *The combined finite-discrete element method*. John Wiley & Sons, Ltd, 2004.

[41] A Viré, J Xiang, and CC Pain. An immersed-shell method for modelling fluid–structure interactions. *Philosophical Transactions of the Royal Society of London A: Mathematical, Physical and Engineering Sciences*, 373(2035):20140085, 2015.

[42] P. Yang, J Xiang, F. Fang, D Pavlidis, J. Latham, and C.C. Pain. Modelling of fluid-structure interactions for multiphase viscous flows via an immersed-shell method. *to be submit to Journal of Computational Physics*, 2015.

[43] Cameron Tropea, Alexander L Yarin, and John F Foss. *Springer handbook of experimental fluid mechanics*, volume 1. Springer Science & Business Media, 2007.

[44] Grady Barrett Wright. *Radial basis function interpolation*: *numerical and analytical developments*. PhD thesis, University of Colorado at Boulder, 2003.

[45] Jiansheng Xiang, Antonio Munjiza, and John-Paul Latham. Finite strain, finite rotation quadratic tetrahedral element for the combined finite–discrete element method. *International journal for numerical methods in engineering*, 79(8):946–978, 2009.

[46] John-Paul Latham, Julian Mindel, Jiansheng Xiang, Romain Guises, Xavier Garcia, Chris Pain, Gerard Gorman, Matthew Piggott, and Antonio Munjiza. Coupled femdem/fluids for coastal engineers with special reference to armour stability and breakage. *Geomechanics and Geoengineering: An International Journal*, 4(1):39–53, 2009.

[47] Qinghua Lei, John-Paul Latham, Jiansheng Xiang, Chin-Fu Tsang, Philipp Lang, and Liwei Guo. Effects of geomechanical changes on the validity of a discrete fracture network representation of a realistic two-dimensional fractured rock. *International Journal of Rock Mechanics and Mining Sciences*, 70:507–523, 2014.

[48] Qinghua Lei, John-Paul Latham, Jiansheng Xiang, and Chin-Fu Tsang. Polyaxial stress-induced variable aperture model for persistent 3d fracture networks. *Geomechanics for Energy and the Environment*, 1:34–47, 2015.

[49] Pain CC, Piggott MD, Goddard AJH, and et al. Three-dimensional unstructured mesh ocean modelling. *Ocean Modelling*, 10:5–33, 2005.

[50] Colin J Cotter, David A Ham, Christopher C Pain, and Sebastian Reich. LBB stability of a mixed Galerkin finite element pair for fluid flow simulations. *Journal of Computational Physics*, 228(2):336–348, 2009.